We are IntechOpen,
the world's leading publisher of
Open Access books
Built by scientists, for scientists

4,800
Open access books available

122,000
International authors and editors

135M
Downloads

Our authors are among the

154
Countries delivered to

TOP 1%
most cited scientists

12.2%
Contributors from top 500 universities

CLARIVATE ANALYTICS

BOOK
CITATION
INDEX

INDEXED

WEB OF SCIENCE™

Selection of our books indexed in the Book Citation Index
in Web of Science™ Core Collection (BKCI)

Interested in publishing with us?
Contact book.department@intechopen.com

Numbers displayed above are based on latest data collected.
For more information visit www.intechopen.com

X-ray Micro-Tomography as a New and Powerful Tool for Characterization of MgB$_2$ Superconductor

Gheorghe Aldica[1], Ion Tiseanu[2], Petre Badica[1],
Teddy Craciunescu[2] and Mattew Rindfleisch[3]
[1]National Institute of Materials Physics, Magurele, Ilfov, 077125
[2]National Institute for Lasers, Plasma and Radiation Physics, Magurele, Ilfov, 077125
[3]Hyper Tech Research, Inc. Troy, OH 45373
[1,2]Romania
[3]USA

1. Introduction

Applied superconductivity is virtually important for all human activities solving different problems in the fields such as power and energy, electronics, computing and communications, medical equipment and sensors, fast transportation and so on. However, the progress in this field is relatively slow when compared to other young industries. The reasons are diverse, and among them are the prohibitive prices vs. performance of the superconducting technologies. In this regard, superconducting-based materials or products with improved working characteristics at constant or lower prices are always of interest.

One superconductor of practical interest is MgB$_2$. This superconductor has several advantages as follows:

1. Critical temperature T$_c$ = 39 K of MgB$_2$ [1] is the highest among simple superconducting compounds. This is a unexpectedly high T$_c$ and, although MgB$_2$ can be considered a s-wave classical Bardeen-Cooper-Schriffer (BCS) superconductor, it shows elements of unconventional superconductivity: two-gap superconductivity was observed with gap values of Δ_σ = 7.4 meV and Δ_π = 2.1 meV at 4.2 K corresponding to critical temperatures of 15 K and 45 K, with σ and π being the bands of the boron electrons [2]. In fact, there are two hole-type quasi-two-dimensional σ bands (σ1 and σ2), an electron-type (π 1) and a hole-type (π 2) three-dimensional π bands [3,4]. Such situation generates new physical effects with markedly different behaviors in many properties some of them of practical meaning when compared with single band superconductors.
2. It is a simple compound composed of only two elements.
3. It is a cheap compound composed of relatively cheap and available elements.
4. It is not toxic and it is considered stable in the air.
5. It is a light compound with low theoretical density of 2.63 g/cm^3. Crystal structure is relatively simple of layered hexagonal type.
6. It has anisotropy, but it is not as high as in high temperature superconductors.

7. Ginzburg-Landau coherence length along the ab-plane is ξ_{ab} = 10 nm, while along c-axis is ξ_c = 5 nm [5]. These values are significantly higher than for the HTS resulting in transparent grain boundaries for the supercurrent passing. Moreover, grain boundaries are recognized to act as strong pinning centers in this superconductor enhancing critical current in high magnetic fields.

8. MgB_2 has in dirty C-alloyed MgB_2 thin films H_{c2} and J_c above the values for the practical superconductors Nb_3Sn and $NbTi$.

9. Films of MgB_2 were shown to grow on single crystal substrates, but also on metallic ones, e.g. on stainless steel [6 and therein refs]. This is important for fabrication of coated conductors.

Despite significant advantages, MgB_2 has several problems in the growth and properties control. Among them we shall mention the fact that Mg is a highly volatile element. High volatility of Mg, according to general ceramic principles does not allow synthesis of high-density bulks. This is a serious and difficult-to-remove limitation and, as a consequence, it requires much effort to improve connectivity, to produce a high-density uniformity and finally to improve critical current density J_c, that is the key parameter for applications of superconductors. Challenging difficulties are amplified because microscopy techniques such as optical microscopy or SEM, in many cases, cannot provide useful information on specifics of the MgB_2 nanostructure, on local density, local density distribution and connectivity, while TEM is very local and is applied to few selected regions. It is important to mention in this context that most of the practical MgB_2 samples are composed of nanoparticles usually less than 20-30 nm. The requirement of nanostructuring in MgB_2 is due to point 7, above introduced: smaller grain in the material means more grain boundaries with a positive effect on pinning increase, and, hence, on J_c enhancement. Another limitation is that typical microscopy techniques are not suitable for 3D observations. On the other hand, 3D observations are extremely useful in analysis of composite complex 3D objects such as wires, tapes, cables, joints, coils and so on of superconductors and in particular of MgB_2. X-ray microtomography as it will be shown in this chapter can fill the gap and solve some of the presented problems, bringing new and very useful information about MgB_2. At the same time X-ray microtomography cannot replace existing microscopy techniques.

2. Principles of X-ray micro-tomography method

Computed tomography (CT) is widely used in the medical community and is receiving increased attention from industrial users including electronics, aviation, advanced materials research, casting and other manufacturing. Computed tomography systems are usually configured to take many views of the object in order to build a 3-D model of its internal structure. 2-D slices through this volume can be viewed as images, or the 3-D volume may be rendered, sliced, thresholded and measured directly. Amplitudes of the volume elements (or voxels) are proportional to the X-ray linear attenuation of the material at that position and are therefore dependent only on material properties and not on the shape of the object as in case of plain radiography.

The principle of most common transmission tomography configurations is depicted in Fig 1. Traditionally, volumetric image reconstruction is achieved through scanning a series of cross-sections (slices) with a fan-shaped X-ray beam, and by stacking these slices. Recently, with the introduction of planar detectors, computed tomography began a transition from fan-beam to cone-beam geometry. In cone-beam geometry the entire object is irradiated with

a point-shaped X-ray source, and the radiation attenuation is measured on a detector plane behind the object. The primary advantages of cone-beam geometry include reduced data acquisition time, improved image resolution, and optimized photon utilization. Cone-beam X-ray microtomography is used in this work to characterize MgB₂ superconducting objects.
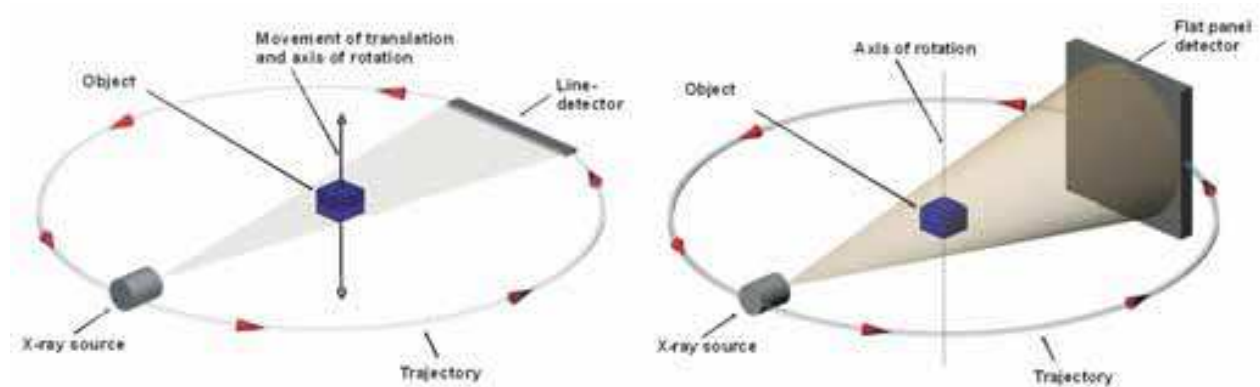

Fig. 1. Fan beam (left) versus cone beam (right) tomography configurations.

Despite progress in exact cone-beam reconstruction, approximate cone-beam reconstruction remains the 3-D CT main solution, especially in the cases of incomplete scanning and partial detection. Furthermore, approximate reconstruction is usually associated with higher computational efficiency, and may produce less image noise and ringing. The Feldkamp (FDK) cone-beam algorithm [7], which is an ingenious adaptation of the weighted filtered backprojection algorithm for equispatial rays, represents the most reliable approach for solving the cone-beam reconstruction problem. The unknown distribution function at position *(t,s,z)* is given by:

$$f(t,s,z) = \frac{1}{2}\int_0^{2\pi}\frac{D_{SO}^2}{(D_{SO}-s)^2}\int_{-\infty}^{\infty}P_\beta(Y,Z)h\left(\frac{D_{SO}t}{D_{SO}-s}-Y\right)\frac{D_{SO}}{\sqrt{D_{SO}^2+Y^2+Z^2}}d\beta dY$$

where: $t = x\cos\beta + y\sin\beta$, $s = -x\sin\beta + y\cos\beta$, *(Y, Z)* are the detector pixel coordinates in a plane translated such that the q-axis is superimposed on the z-axis (Fig. 2).

The cone beam reconstruction algorithm can be conveniently broken into the following steps:

1. Weighting projections: multiply projection data, *Pβ(Y,Z)*, by the function *Dso/(Dso²+Y²+Z³)* to find the weighted projections.
2. Filtering projections: convolute the weighted projection with the ramp filter h by multiplying their Fourier transforms with respect to Y. Note this convolution is done independently for each elevation Z.
3. Backprojection: each filtered weighted projection is backprojected over the three-dimensional reconstruction grid. The two arguments of the weighted projection represent the transformation of a point in the object volume into the coordinate system of the tilted fan.

The FDK algorithm is highly parallelizable and hardware supported. The FDK is an approximate method because only those points of the object that are illuminated from all directions can be properly reconstructed. In a cone-beam system this region is a sphere of radius $D_{SO}\sin(\Gamma_m)$ where Γ_m is half the horizontal cone angle. Outside this region a point

will not be included in some of the projections and thus will not be correctly reconstructed. The main limitation occurs at relatively large cone angles.
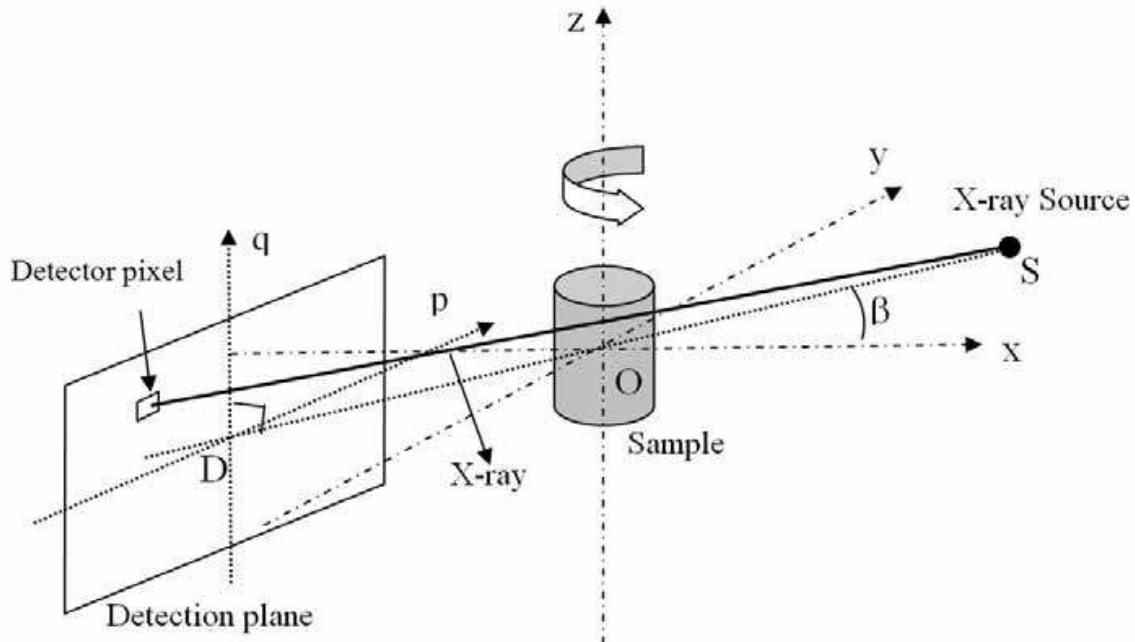

Fig. 2. Feldkamp algorithm cone-beam geometry

Oxyz   - reconstruction coordinate system; sample rotates around z-axis
Dpq   - planar detector coordinate system
SO   - source-object distance
SD   - source-detector distance
β   - angle of rotation of sample (equivalent picture – angle of synchronous rotation of source-detector assembly)

The application of X-ray tomography for non-destructive analysis of superconducting materials was recently reported. Synchrotron tomography [8-9], but also micro-tomography based on conventional X-ray tubes [10, 11] proved to provide useful information on the internal structure of superconducting materials. X-ray micro-tomography (XRT) was initially used and tested to reveal in a non-invasive and convenient way [11], the architecture of the superconducting composite wires. The method can also reveal at macro local scale the occurrence, distribution and shape of the regions with a different density [12]. The results presented here were obtained using a high resolution X-ray micro-tomography facility constructed at NILPRP Bucharest, Romania with European Community support. The main component is an open type microfocus X-ray source (W target, maximum high voltage of 160 kVp at 20 W maximum power). X-rays are detected by means of a high-resolution image intensifier (Siemens Medical Solutions) or an amorphous silicon flat panel sensor (Hamamatsu). The detection system is placed on a precise motorized stage (Sigma-Koki) additionally provided with vertical and transversal adjustable tables. The investigated sample is placed on a four axes motorized manipulator to assure a high degree of freedom in accurate sample positioning. The micro-radiography analysis is guaranteed for feature recognition down to 1 micron. Due to the ability to work with magnifications over 1000, it has been demonstrated that for miniaturized samples the micro-tomography analysis is valid for feature recognition down to few microns. The 3D tomographic image

reconstructions are obtained by a proprietary highly optimized computer code based on a modified Feldkamp algorithm.

The reconstruction software also incorporates efficient techniques for beam hardening reduction and ring artifacts elimination. Beam hardening effects are the main challenge for the application of the microtomography technique to the analysis of high density metallic samples. Beam hardening artifact consists of an elevated density displayed on the perimeter of a uniform density object and a corresponding density depression in the object's core region. It is caused by the polychromatic structure of the energy spectrum of the X-ray generators. Several experimental techniques have been reported for beam-hardening correction [13-15]. However, the optimization of the tomographic measurement by experimental selection of a large set of parameters is a very laborious procedure and the result is not always guaranteed. Therefore, in our approach [15], a numerical simulation procedure-time-independent multimaterial and multidimensional-coupled electron/photon Monte Carlo transport - was developed. Any important element, such as: target material, pre and post-filters and X-ray energy spectra have been studied. The optimisation procedure requires pre-filtering the X-ray beam for narrowing the energy spectra, at the same time monitoring the spectra evolution into the probe structure for maximum absorption contrast. High performance microtomography on fusion material samples of advanced steel alloys would require, in addition to beam parameters optimization, the application of active methods of beam hardening reduction. This means the determination of the non-linear dependence between investigated object thickness and log ratio of intensities in the radiographic views, followed by the corresponding processing of the radiographic data. Obviously, determination of the non-linearity of the line integrals by accurate Monte Carlo simulation instead of laborious experiments is always desirable. Reducing beam hardening effects means, consequently, reducing the need for employing highly sophisticated post-processing methods.

3. Application of XRT on MgB$_2$ superconductors

3.1 MgB$_2$ synthesis using mechanical alloying method and X-ray microtomography observations

First attemps to apply X-ray microtomography were performed on MgB$_2$ ceramic obtained by conventional solid state reaction between powder of boron and magnesium. Mixtures of Mg (99.5%, 45 μm), B (0.85 μm, amorphous, 95% purity and impurities are: 3% Mg, 0.5% water soluble, 1% insoluble in H$_2$O$_2$ and 0.5% moisture) and SiC (99.3%, 20 nm) powders with composition (Mg + 2B)$_{0.95}$(SiC)$_{0.05}$ were prepared by hand mixing under Ar (glove-box) and by mechanical milling in a planetary ball mill (Fritsch P7, Cr-steel pot and 20 balls of 7 mm diameter; composition of the Cr-steel used for the pot and balls is: 85.3%Fe, 12%Cr, 2.1%C, 0.3%Si, 0.3Mn) [16, 17]. Mechanical milling was done for 0.5, 1, and 3 h at 400 rpm under Ar gas introduced into an evacuated milling pot. As-prepared powders, after pressing into pellets, were heat treated in Ar using a tube furnace with a quartz tube. Pellets were wrapped into Mo and Zr-foils together with chunks of Mg to prevent significant evaporation of this element from the samples during heating. Samples and processing conditions are gathered in Table. 1.

Samples were characterized by x-ray diffraction (PANalytical, CuKα radiation) and SEM (JEOL JSM 6400F). Measurements of M-H loops at 4.2 K and 20 K were conducted using a

SQUID magnetometer (Quantum Design, 5T). Same equipment was used to determine critical temperature, T_c taken as the onset of the diamagnetic signal in the zero-field-cooled M(T) curves measured for a *dc* magnetic field of 20 Oe. X-ray microtomography measurements were performed as presented in second part of this section.

Sample	Mixing/milling	Heat treatment temp. (°C)	Heat treatment time (h)
A	Manual in Ar	700	1h
B	Mechanical milling in Ar, 0.5h	700	1h
C	Mechanical milling in Ar, 1h	700	1h
D	Mechanical milling in Ar, 3h	700	1h
Tape	Powder in tube MgB_2 tape [18]	750	1h

Table 1. Samples and processing conditions

SEM images (not presented) taken on the A-D Ar-as-milled (un-reacted) powders consist of large agglomerates up to 30-50 μm and no other significant differences can be observed. On the other hand, XRD patterns for the same precursor powders A-D show that enhancement of milling time produces patterns with Mg diffraction-lines of lower intensity and larger *full width at half maximum* (FWHM). For A-D mixtures FWHM was estimated at 0.16, 0.23, 0.25 and 0.27°, respectively. The result suggests occurrence of smaller particles with a lower degree of crystal perfection for Mg vs. milling time. A relatively short milling time leads to a relatively fast decrease of the intensity and a fast increase of FWHM, while for longer milling time variation of the intensity and of FWHM is slower. B cannot be observed in the XRD patterns since this element was used in the amorphous state.
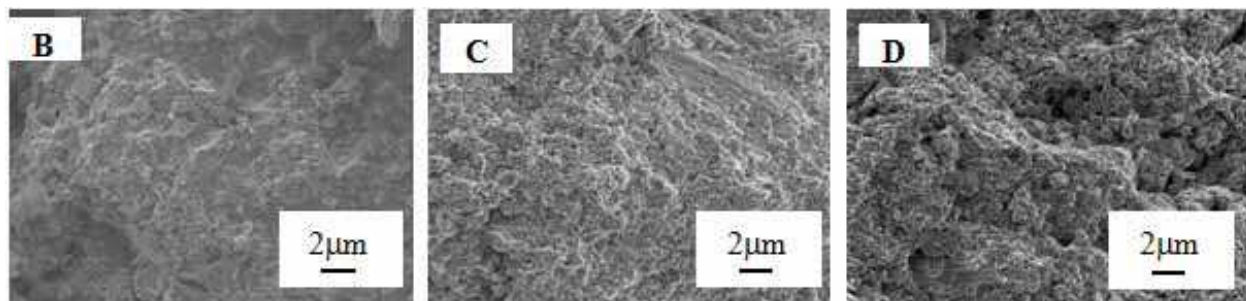

Fig. 3. SEM images for the reacted B-D samples. Sample notation is the same as in Table 1.

Bulk samples prepared from the powders A-D for the same heat treatment conditions are showing roughly very similar XRD and SEM (Fig. 3) results with some small differences. In the XRD the crystal quality is decreasing with the milling time, but the ratio between different phases is approximately constant. Low level of MgB_4 in the samples indicates that Mg-losses during heat treatment are relatively low, while the decrease in *a*-axis of the MgB_2 (from 0.3084 to 0.3074 nm) with the increase in the milling time (from 0 to 3 h, respectively) of the precursor mixtures suggests introduction into the lattice of MgB_2 of C coming from the milling pot and balls.

SEM images (Fig. 3) on the reacted B-D samples are showing small grains and agglomerates of 1-3 μm. The appearance is of a glassy bulk where the grains cannot be easily observed, and the connectivity between the grains is likely decreasing from sample A to D. The

decrease of the connectivity and the decrease of the crystal quality can be the reasons for the decrease of the superconducting properties. Carbon presence should be also considered and it is probably the main reason for the observed decrease of the critical temperature (37.4, 34.8, 32.2 and 32 K for A-D samples, respectively). The presence of other impurities is also of interest and some aspects are addressed in the next paragraphs. The decrease in T$_c$ with the milling time is accompanied by the decrease in the magnetization loop width, ΔM, which is proportional to J$_c$ through the Bean formula [19] (Fig. 4).

Our results indicate that milling and milling time are important and are producing different states for Mg and a different level of carbon in the precursor. This likely influences the further growth processes leading to a different quality of the MgB$_2$ samples. Changes in the superconducting properties are logically correlated with the changes observed in SEM and XRD data, but the details are missing and the mechanism and the key factors controlling this relationship cannot be satisfactorily revealed. It is also questionable if this is the full picture and one problem is that the changes in the T$_c$ and J$_c$ are significant, while in the XRD and SEM are much lower. This discrepancy leads to the idea that XRD and SEM are not sensitive enough or are not the most appropriate to reveal the differences. Complementary techniques to check and expand the available data are needed.
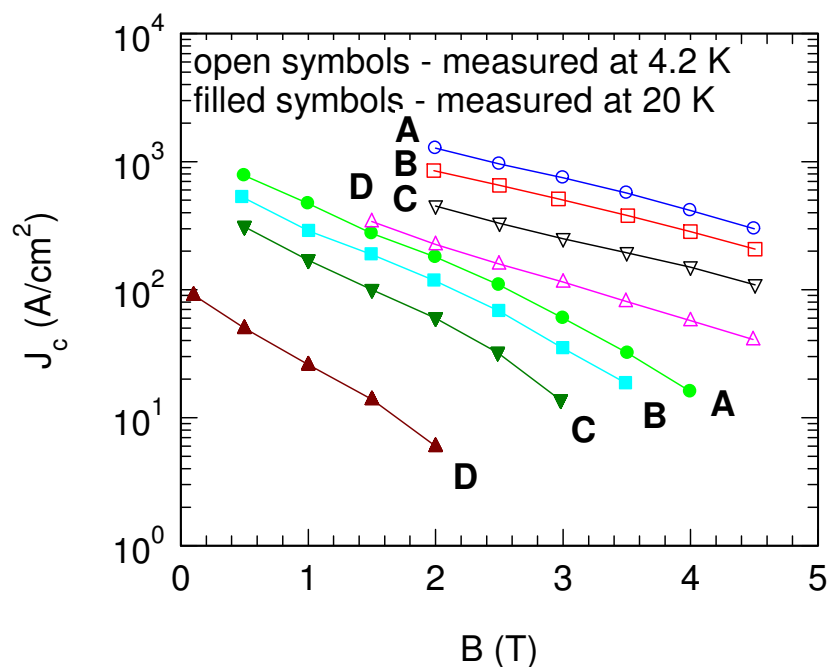

Fig. 4. Magnetization loop width (proportional to J$_c$) for the samples A-D at 4.2 K and 20 K.

X-ray microtomography (XRT) was applied for characterization of the reacted bulk samples AD (Fig. 5). This technique can display images of microstructure in the sense that the dark regions are of low density. Pores in the material will be black and they will have the shape and size as visualized through microscopy. Grains will have in the XRT images different gray tones and the whiter they are the higher density they have. What is remarkable about this technique is that, in fact, we do not depend on the clear observation of the grains to construct a 3D image showing macroscopic regions of the material with a different density.
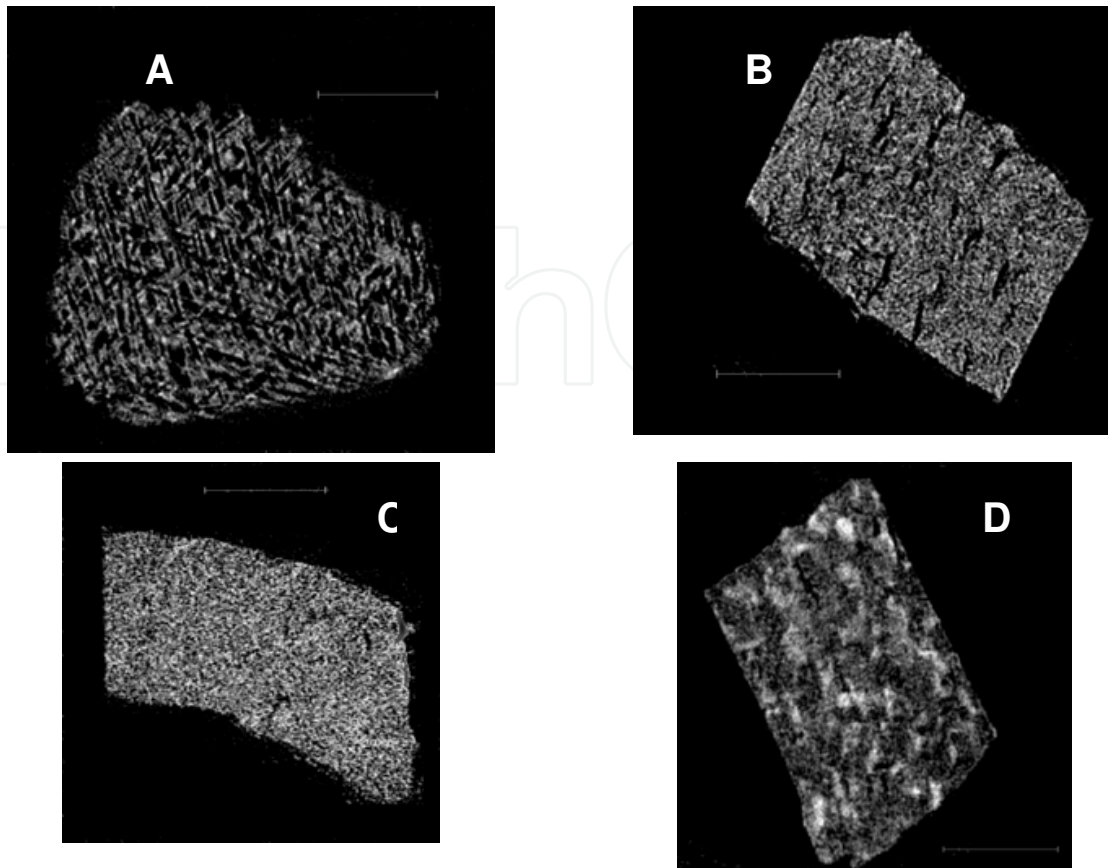
Fig. 5. Representative XRT images of the heat treated bulk samples A-D (Table 1). Images were taken for a voltage of 40 kV and a current of 100 μA. Scale bar is 100 μm.

This is advantageous because even a relatively low XRT resolution (of few μm in our case) when compared to SEM or TEM and when measuring materials composed of small-size grains (for our samples less than 50-100 nm and significantly less than the XRT resolution), can reveal useful information on local density distribution and uniformity or on the shapes, packing and alignment of the regions and/or pores of the size larger than the resolution. Further development of the technique and improvement of the resolution is expected to show more details inside the macroscopic regions and also to identify the phases based on their density. One interesting aspect related to the last part of the previous statement is that our MgB_2 samples contain a relatively low level of impurities. By XRD the impurities in the reacted A-D samples were Mg_2Si, MgO, MgB_4 and some unreacted Mg. The densities, d, of different phases in the material and of the raw materials are: d_{SiC} = 3.22 g/cm^3, $d_{C\text{-graphite or amorphous}}$=1.8-2.3 g/cm^3, d_{Mg} = 1.738 g/cm^3, $d_{B\text{-amorphous or crystalline}}$ = 1.74-2.44 g/cm^3, d_{MgB2} = 2.63 g/cm^3, d_{MgO} = 3.58 g/cm^3, d_{Mg2Si} = 2.56 g/cm^3 and d_{MgB4} = 2.50 g/cm^3. The highest density is for MgO or SiC. The two phases should have the whitest colour on the XRT images. The amount of the XRT white regions in the A-D superconducting samples is much larger than a few percent of residual MgO or SiC phases estimated from XRD. Hence, the white regions in the XRT images do not reflect a certain phase and mainly show regions with a very different local density. However, contribution of a certain phase to the colour nuance of a region cannot be totally excluded. It is also necessary to discuss some other issues related to the limitations of different measurement techniques. It is generally recognized that solid and liquid phases are present during the reaction to form MgB_2.

Hence, glassy phases, phases with poor crystal quality or nanoscale grains can easily occur and can be hardly detected by XRD leading to underestimated values of the impurity-phases amounts. Following the same idea, a special attention deserves MgO or more general the presence of oxygen in the material. Sometimes, a fine mixture of MgB$_2$ with oxygen is mentioned (more often for thin films), and even by high resolution techniques such as TEM it is very difficult to observe grains of MgB$_2$ and MgO and to make a separation between them. Since the role and behaviour of the oxygen in MgB$_2$ is not clear and also considering the above limitations from the different measuring techniques it is wise to keep in mind the oxygen impurification during milling and the following scenario can be imagined: with the increase in the milling time, the amount of oxygen impurification in the precursor powders may increase. This might be related to the behaviour of Mg and its reactivity influenced by the milling conditions. It is thought that longer milling time, generating lower Mg crystal quality and smaller grains, leads to more reactive powders including with residual oxygen. It is noteworthy that, during milling, other processes relevant for the XRT images may take place such as the transfer of the material from the milling-pot-walls and balls into the precursor powder. Impurities are also present in the raw materials, especially in the boron amorphous raw powder of relatively low purity. Milling can change their behaviour so that they can influence processes. However, EDS and XRD investigations could not detect impurity elements (except the presence of C entering the lattice of the MgB$_2$ phase) or phases (such as Fe$_2$B) in the MgB$_2$ final bulk meaning that, if they are present, these elements are below the detection limit of these techniques. From XRT point of view changes in the particle size and particle size distribution can influence agglomeration and rheological properties of the powder mixtures so that packing and density distribution in the bulk can be very different.

Although, at present, it is not possible to significantly advance the understanding of the milling-properties relationship, XRT can reveal clear differences between the samples and the details are addressed in the next paragraphs.

For the reacted samples milled in Ar-atmosphere (Fig. 5), XRT microstructure is changing from a vermicular in A to a layered structure with long oriented pores in B (up to 50 μm in length), to a relatively uniform distribution of the regions of higher and lower density and containing many small pores as well as few large pores of irregular shape in sample C. Finally, a 'leopard'-3D-spot-like structure is observed for the sample D. The white 'spots' of the high density material in this sample are of regular sphere- and ellipsoidal- like or of the irregular shape. One can appreciate from the Fig. 5 that the amount of the brighter regions is likely to enhance from A to D and, hence, the amount of the high density regions in the material is enhancing. At the same time the homogeneity of the samples is getting lower. Furthermore, the tendency of the XRT patterns is likely preserved for the case when precursor powders are milled in H$_2$ atmosphere [12], but the evolution of the XRT microstructure towards the 'leopard'-like structure is slower. This might be because Ar is an inert atmosphere while H$_2$ is a highly reducing one, so that the reacted samples in the same conditions may contain different amounts of the residual oxygen, as it was discussed above.

3.2 Observation of MgB$_2$ tapes and wires by XRT

Powder-in-tube fabrication of the tape observed by X-ray microtomography was reported in [18].

XRT structure of the tape can be visualized in (Fig. 6). Tape shows relatively uniform XRT microstructure, when compared with the patterns taken on bulk samples A-D (Section 3.1),

but one can easily observe regions with different nuances of gray. There are regions in the center of the MgB_2 core from the tape that are darker (e.g. see Fig. 6c) suggesting a lower density, and meaning, from a practical point of view, that that there is room for improvements even for tapes with record high level of J_c in high magnetic fields [18] as measured in this tape investigated here by XRT.
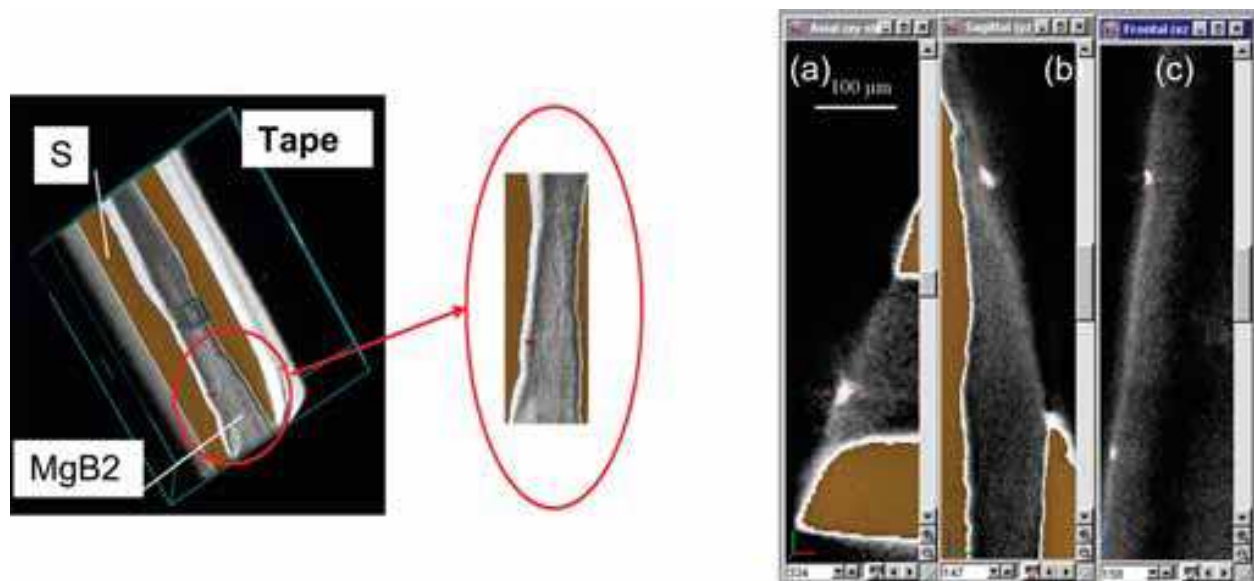

Fig. 6. 3D XRT image reconstruction of an MgB_2 tape (S = metal sheath) and representative images of the (a)- axial, (b)-sagital and (c)-frontal (from left to right) sections. The cross identifies the same point in all images. Images were taken for a voltage of 60 kV and a current of 80 μA.

Apart from the local density information, 3D images and selected sections can also give valuable information on the architecture and geometrical perfection of the composite tapes or wires as well as on some macro defects such as cracks and pores.

3D visualisation is particularly important for complex multifilamentary MgB_2 wires. This is because for real applications (e.g. fabrication of the superconducting coils) wires are more suitable than tapes. This situation, and the necessity to test the 3D geometrical quality and defects of the wires for their further improvement and for development of new types of wires, motivated us to apply XRT visualization to commercial wires produced by HyperTech Inc, US. These round-shape wires of MgB_2 were produced by Hypertech Inc. by continuous tube forming and filling process [20].

The significant advantage of XRT in the case of wires is that it works on extended 3D volumes vs. 2D SEM or optical microscopy. The 3D reconstructed images can reveal hidden defects that can easily go unnoticed with traditional microscopy methods. For example, in Fig. 7, from the SEM images taken in SE and BSE regimes on a HyperTech wire with 7 sub-elements, one can observe regions with possible defects. The nature, shape and, hence, importance of such defects cannot be assesed from the 2D images. At the same time, 3D navigation (Fig. 8 left) inside the same wire shows macrodefects. In particular, defects of interruption of the Nb barrier material or voids are clearly visible. Similar 3D defects were visualised for another HyperTech wire with 18 sub-elements (Fig. 8 right). Macrodefects, such as e.g. voids, can have extended, irregular shape and, not rarely, a hidden part. It

means that XRT is valuable not only because it is possible to detect the defect in a highly reliable way, but it can reveal their 3D shape details.
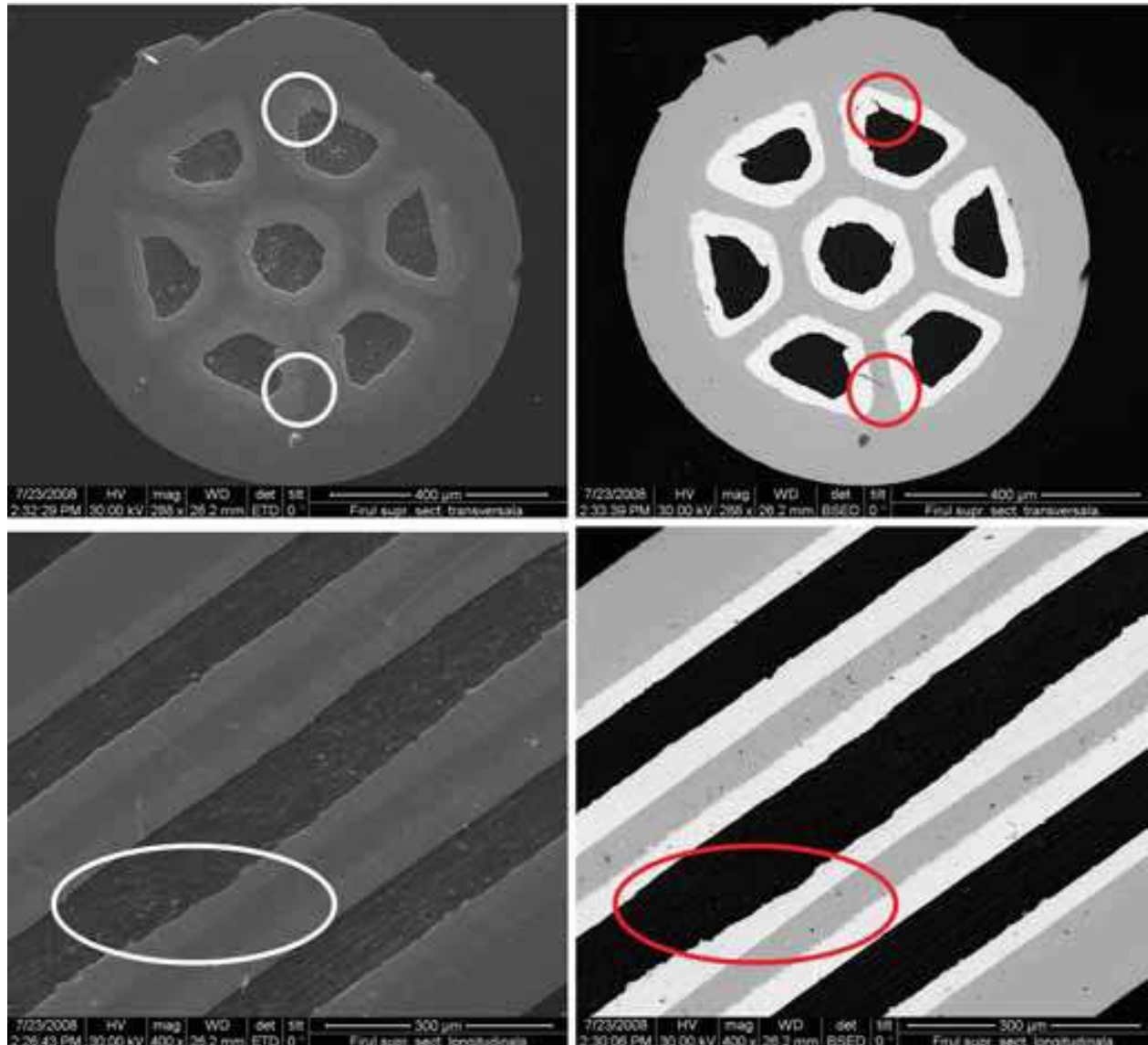

Fig. 7. SEM images of the polished Hypertech MgB$_2$ wires (7 sub elements): upper panels – transversal SE and BSE modes; bottom panels - longitudinal SE and BSE modes. Defects are identified by the circles. The outer diameter of the wire is 0.83 mm.

It is expected that different architecture of the wires will result in different non-uniformities leading to different overall quality. Non-uniformity is expressed in uniformity of the phase quality (crystal, morphological, structural defects, impurities, grain boundaries) density distribution quality (variation of the local density as discussed for tapes), geometrical perfection. It is a complex system and indicated parameters are not independent. Architecture of the wire vs. processing should be investigated and optimized. XRT can help in understanding the geometrical quality of a sample produced by different technological conditions or it allows comparative analysis between different wires for the same technology. For example, the two wires already mentioned (Fig. 8 left and right colums) from the geometrical perfection viewpoint, even in the absence of the macrodefects are very

different. For each wire there is a difference in the quality of the superconducting sub-elements if the sub-element is located in the outer or inner part of the wire. Namely, interface roughness (R) between Nb and MgB_2 sub-element for the inner sub-elements is higher, while cylinder-shape perfection (CSP) is worse for the same sub-elements. Furthermore, this difference between inner and outer sub-elements is higher for the wire with 18 than for the wire with 7 sub-elements. A closer look also suggests that the worst quality from the R and CSP viewpoints is for the inner sub-elements from the wire with 18 sub-elements. These representative results show that XRT analysis can play an important role in explaining the differences in superconducting properties of MgB_2 samples. However, at present, the relationship between XRT and the superconducting properties of the wires is not established and more research is required.

3.3 MgB$_2$ consolidation by Spark Plasma Sintering method and XRT observations

One promising method to obtain a dense MgB_2 superconductor is the Field Assisted Sintering Technique (FAST), also known as Spark-Plasma-Sintering (SPS) that was successfully used to consolidate different kinds of difficult-to-sinter powders [e.g. 21]. In this technique, the sample is submitted to a pulsed electric field during the compression process. Although the physics involved is not completely understood, this method provides an excellent way to obtain high density MgB_2 [22-24], while preventing the increase of the grain size. Both, high density and reduced grain size, as already noted above, are very important features for maximization of the properties in MgB_2. Also, doping with various elements or compounds into MgB_2 has been found to enhance the critical current properties [25-27]. In this respect, best results were obtained by using nano-SiC [28], SiC whiskers, nanometer Si/N/C [29] and B_4C [30], that showed a positive influence on irreversibility field (H_{irr}) and critical current density J_c under magnetic fields. In this regard detailed study of the XRT microstructure of MgB_2 samples is of interest.

Polycrystalline samples of MgB_2 (MB), C-doped MgB_2 (MBBC), and SiC-doped MgB_2 (MBSC) were prepared from commercially available powders of MgB_2 (2.3 μm, Alpha Aesar), SiC (45 nm, Merck), and B_4C (0.8 μm, HC Starck Grade HS). For each experiment about 3 g of MgB_2 powder without or with doping compound was loaded into a graphite die with 1.9 cm diameter punches. Prior to powder loading, MgB_2 and SiC or B_4C were mixed in a 0.95:0.05 molar ratio using a mortar and pestle in argon atmosphere for 30 min. After loading the powder into the die (also in argon atmosphere), samples were processed using a "Dr Sinter" (Sumitomo Coal Mining Co, Japan) sintering machine. Sintering was performed in vacuum (6-15 Pa). The temperature was measured by a thermocouple (type K) placed at half of the thickness of the die wall. A uniaxial pressure of 63 MPa was applied during sintering for all samples. In the SPS apparatus, we used a default 12:2 (on:off) current pulsed pattern. The waveform is not square and, in fact, is composed of several spikes (pulses) separated by a current-free interval [31]. Regardless of the pattern, each pulse has the same period of about $3 \cdot 10^{-3}$ s. Thus, the pattern of 12:2 has a sequence of 12 pulses "on" and 2 pulses with no current (off). The total time of one sequence (cycle) is about 0.04 s. The operating voltage and the peak current were below 10 V and 1000 A, respectively.

The SPS-processed pellets have bulk densities (Table 2) above 90 % of the theoretical value (2.63 g/cm^3) [32, 33]. For $0.95MgB_2+0.05B_4C$ a smaller density is observed probably due to the limited chemical reaction between two components, and to a lower sintering temperature. Maximum sintering temperature was selected to be about 40-45 °C higher then the temperature T_d where sample's densification starts.
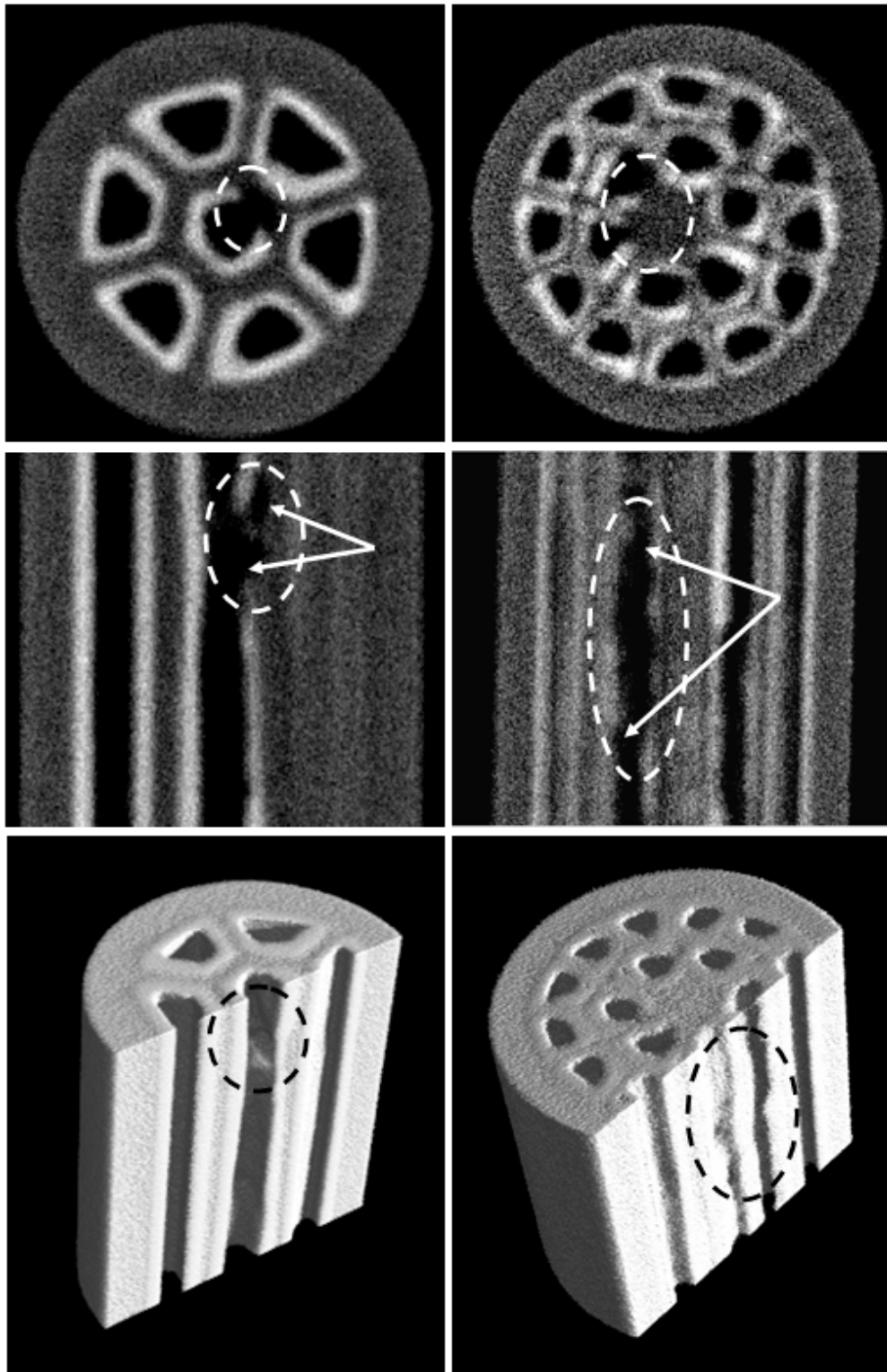
Fig. 8. X-ray microtomography images of the Hypertech MgB$_2$ wires: left panels - 7 sub elements; right panels - 18 sub elements. Defects are identified on transversal (top) and longitudinal (middle) cross sections and on the associated 3D reconstructions. The outer diameter of the wires was constant at 0.83 mm.

Sample	T (°C)	Density (g/cm³)	T_d (°C)
MB	960	2.39	920
MBSC	1000	2.37	955
MBBC	1000	2.08	960

Table 2. Samples, the maximum SPS-processing temperature, final density and T_d data.

The tomographic inspection was performed using the following operation parameters: U = 50 kV, I = 40 mA, voxel size = 5 μm. Representative results on the pristine MgB_2 sample are presented in Figs. 9-11. Figure 9 illustrates the identification of high density regions inside the investigated sample. By filtration and thresholding techniques the distribution of these high density regions inside the volume of the sample is revealed in Fig. 10. The identification of macroscopic low density regions is illustrated in Fig. 11.
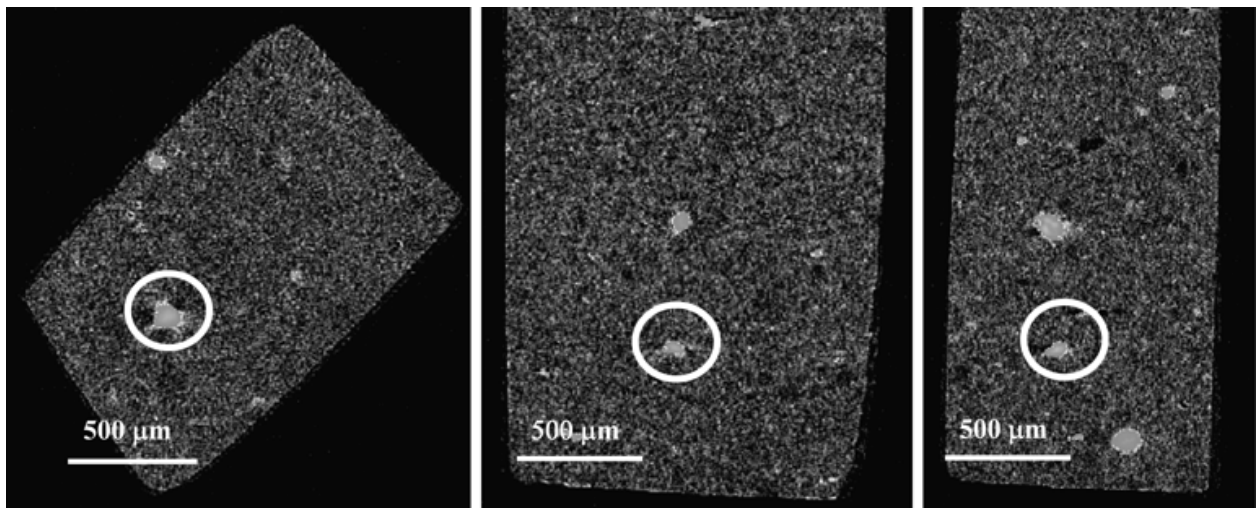
Fig. 9. Transversal, sagital and longitudinal cross-sections revealing high density regions; high density region size (inside circles) is of about 160 μm.
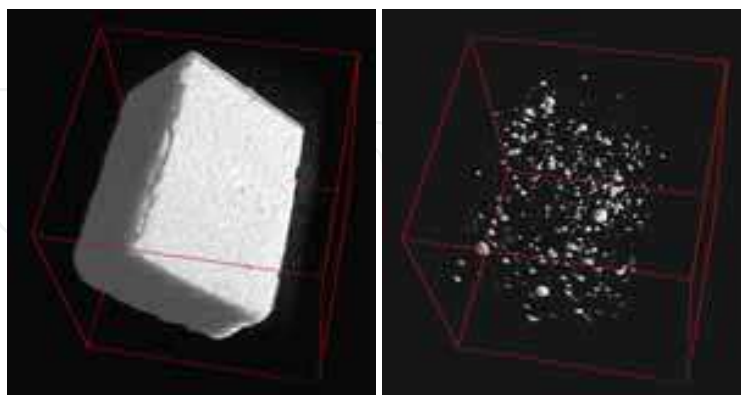
Fig. 10. 3-D reconstruction (left) and the distribution of the high density regions inside the volume of the sample of about 0.8 mm³.

To identify what represent the dense regions, the high resolution X-ray digital radiography analysis was performed on the raw powder sample. The result is presented in Fig. 12. In order to have a dimensional/density reference, a wolfram wire of 5 μm diameter, was

placed on the sample. The radiography reveals high density regions, of above 2-3 μm diameter-size, spreaded in the sample. Same intensity of the W-wire and of the high density regions suggests that in the commercial as-received MgB$_2$ raw powder this element is present, most probably in the form of WC. We suppose that impurification occured during powders milling in the process of commercial MgB$_2$ raw powder preparation.
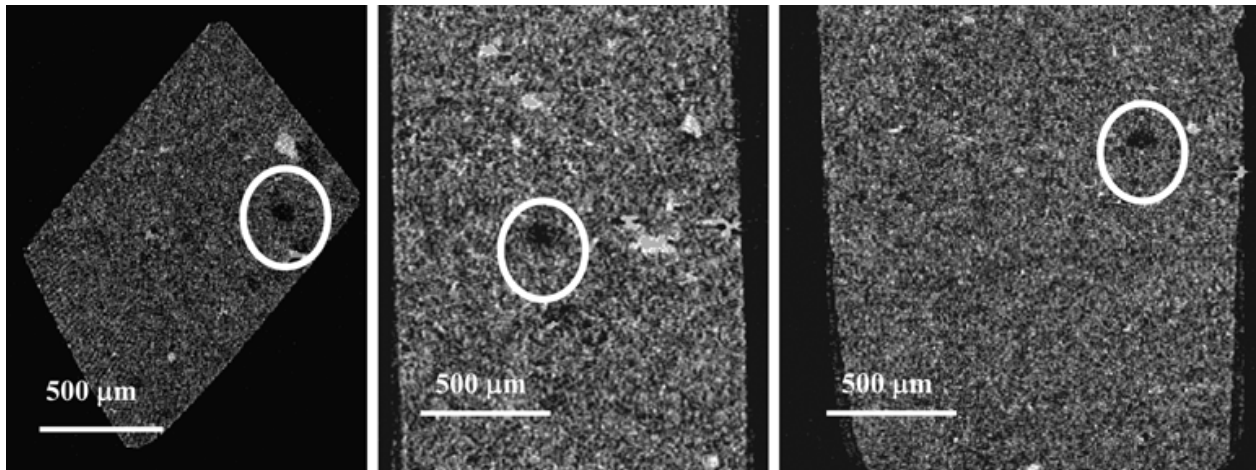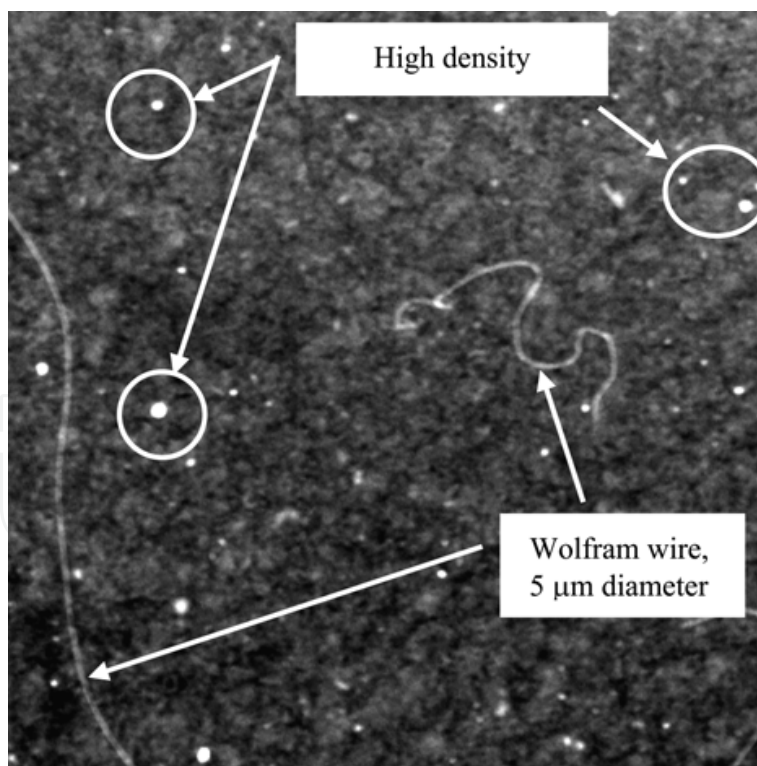

Fig. 11. Transversal, sagital and longitudinal cross-sections revealing low density region; low density region size (inside circles) is of about 130 μm.

Fig. 12. Digital radiography of a MgB2 sample and a W-wire.

For the studies by SEM, for a comparative analysis with micro-tomographic experiments, the samples have been fractured to reveal their grains structure and morphology. Selected secondary electron image is shown in Fig. 13. One can observe dense polycrystalline pristine

SPS-processed MgB2 material with pores and grains of different form and size (Fig. 13). The pores of micrometer order are located at the grain boundaries. Apparently the observable size of the grains or sintered aggregates is of 0.2 – 2.5 μm. There are no significant differences that can be revealed by SEM among the 3 SPS-processed samples.
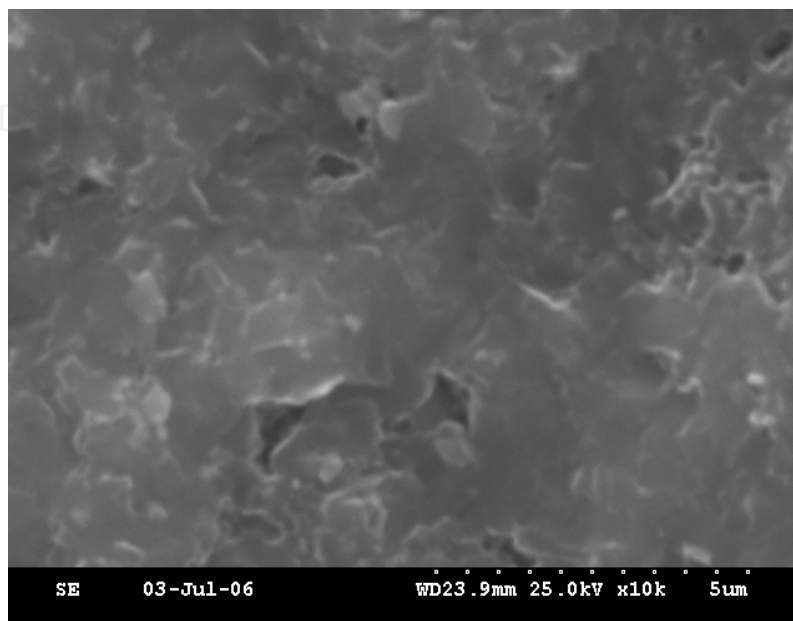

Fig. 13. Polycrystalline MgB_2 sample (×10.000).

Images of 3D tomographic reconstructions were observed in SiC- and B_4C- doped MgB_2 samples. In Fig. 14 it can be observed the diference of the local densities between three samples. Samples show some clear differences, but, they are not as large as in the case of the samples A-D presented in Section 3.1. Remarkable is that although the local density uniformity is much improved for the SPS-processed samples, this is not perfect and a lower quality is likely obtained for the samples with additions. Indeed, some superconducting parameters were superior for the pristine MgB_2 SPS-sample and detailed results were reported in [34].

4. Discussions and future trends

XRT is a useful and powerful technique to observe MgB_2 superconducting samples. Remarkable is that although the resolution is at the level of micrometers we investigated nanostructured MgB_2-based materials, and we got very useful information. We shall emphasize that one important limitation of the XRT is that it cannot give any information on crystal quality and composition. Therefore, this method is providing additional information, but it cannot replace the data from other measurements such as, e.g. structural ones (x-ray or electron diffraction) or those giving quantitative data on local composition (EDS, other). It is expected that with the improvement of the resolution more details can be observed. This is especially important for more uniform samples such as SPS-processed MgB_2-bulks. Such developments are expected also to help in advancing the understanding of the relationship between processing, XRT, conventional microscopy techniques and superconducting properties. Based on this, a new generation of MgB_2 tapes/wires for various applications with optimum, controlled or improved working parameters will be produced.

In this work we show that XRT can reveal in a non-invasive and convenient way the architecture of 3D MgB$_2$ composite objects (e.g. wires). This is an important advantage saving time and energy.
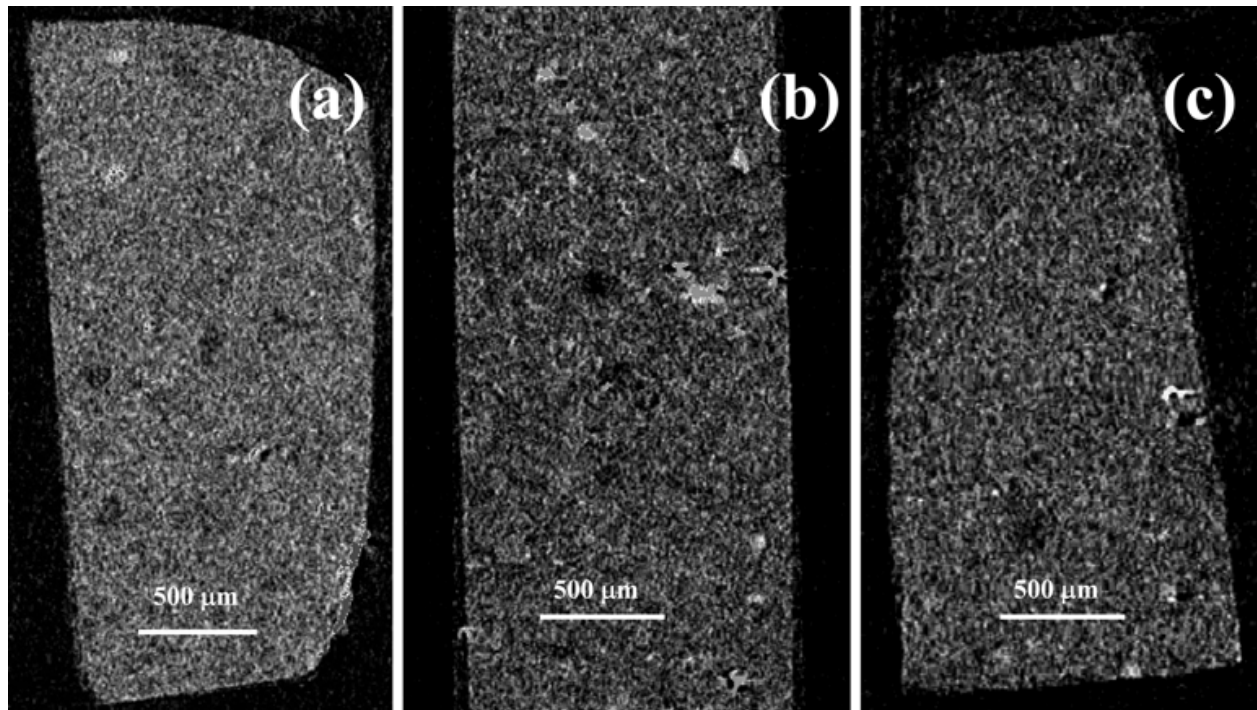

Fig. 14. Sagital cross-sections: (a) MgB$_2$ (MB), (b) SiC-doped MgB$_2$ (MBSC) and (c) C-doped MgB$_2$ (MBBC).

XRT is envisioned as a continuous and in-situ testing method of the quality of the MgB$_2$ bulks, wires, tapes (and in the future of thin films) and their products. For example, XRT will provide direct and real-time information during processing, fabrication or exploatation of a MgB$_2$-based product (e.g. fabrication of composite superconducting wires/tapes, formation of joints, coils winding, coils exploatation and so on).

XRT will bring also information on local chemical and phase composition and some positive results are already in progress.

XRT is not limited to MgB$_2$ and many other classes of materials can be investigated by this method. There is no doubt that XRT will become a key characterization technique in materials science and technology.

5. Conclusion

In summary, we applied XRT vizualization to MgB$_2$ bulks, tapes and wires. XRT provides powerful and unmached information by the conventional microscopy techniques on the local 3D density uniformity and distribution, connectivity, search and identification of the macrodefects, 3D-shape details of the macro defects and of the components from the composite MgB$_2$ wires or tapes, on the roughness and perfection of the intefaces between the components. Advantages, limitations and future development trends are discussed. We have also shown that XRT allows to evaluate at least qualitatively the architectural integrity and geometrical quality of the samples and this information can be related to

superconducting quality of the products. However, the details of this complex relationship remains unrevealed and the expectations are that with the improvement in the 3D XRT method one may understand more in this direction with much benefit in designing and fabrication of improved MgB_2 superconducting products.

The importance of pioneering the application of 3D non-invasive XRT on MgB_2 is general, i.e. XRT is expected to be applied with much success for many other materials, processing and fabrication processes, and to monitor the work of different products/systems.

6. Acknowledgements

7. References

[1] Nagamatsu J, Nakagawa N, Muranaka T, Zenitani Y, Akimitsu J, *Superconductivity at 39 K in magnesium diboride*, Nature 410 (2001) 63.

[2] Picket W, *Mind the the double gap*, Nature 418 (2002) 733.

[3] Yang H, Liu Y, Zhuang C, Shi J, Yao Y, Massidda S, Monni M, Jia Y, Xi X, Li Q, Liu ZK, Feng Q, W HH, *Fully band-resolved scattering rate in MgB_2 revealed by nonlinear Hall effect and magnetoresistance measurements*, Phys. Rev. Lett. 101 (2008) 067001.

[4] Kortus J, Mazin II, Belashchenko KD, Antropov VP, Boyer LL, *Superconductivity of metallic boron in MgB_2*, Phys. Rev. Lett. 86 (2001) 4656.

[5] Caplin AD, Bugoslavsky Y, Cohen LF, Cowey L, Driscoll J, Moore J, Perkins GK, *Critical fields and critical currents in MgB_2*, Superconductor Science and Technology 16 (2003) 176.

[6] Xi XX, *MgB_2 thin films*, Superconductor Science and Technology 22 (2009) 043001 (review).

[7] Feldkamp LA, Davis LC, Kress JW, *Practical cone-beam algorithm*, J. Opt. Soc. Am. A 1-6 (1984) 612.

[8] Haibel A, Scheuerlein C, Synchrotron Tomography for the Study of Void Formation in Internal Tin Nb_3Sn Superconductors, IEEE Transactions on Applied Superconductivity 17(1) (2007) 34.

[9] Scheuerlein C, di Michael M, Haibel A, *On the formation of voids in internal tin Nb_3Sn superconductors,* Appl. Phys. Lett. 90 (2007) 132510.

[10] Tiseanu I, Craciunescu T, Mandache NB, *Non-destructive analysis of miniaturized samples and irradiation capsules by X-ray microtomography*, Fus. Eng. Des. 75–79 (2005) 1005.

[11] Tiseanu I, Craciunescu T, Petrisor P, della Corte A, *3D X-ray micro-tomography for modelling of Nb_3Sn multifilamentary superconducting wires*, Fus. Eng. Des. 82 (2007) 1447.

[12] Badica P, Aldica G, Craciunescu T, Tiseanu I, Ma Y Togano K, *Microstructure of MgB_2 samples observed by x-ray microtomography*, Supercond. Sci. Technol. 21 (2008) 115017

[13] Hammersberg P, Mangard M, *Correction for beam hardening artefacts in computerised tomography*, Journal of X-ray Science and Technology 8 (1998) 5.

[14] Van Geet M, Swennen R, Wevers M, *Quantitative analysis of reservoir rocks by microfocus x-ray computerised tomography*, Sedimentary Geology 132 (2000) 25.

[15] Tiseanu I, Simon M, Craciunescu T, Mandache BN, Volker Heinzel C, Stratmanns E, Simakov SP, Leichtle D, *Assessment of the structural integrity of a prototypical instrumented IFMIF high flux test module rig by fully 3D X-ray microtomography*, Fus. Eng. Des. 82 (2007) 2608.

[16] Kondo T, Badica P, Nakamori Y, Orimo S, Togano K, Nishijima G, Watamabe K, *MgB$_2$/Fe superconducting tapes using mechanically milled powders in Ar and H$_2$ atmospheres*, Physica C 426-431 (2005) 1231.

[17] Badica P, Kondo T, Togano K, Aldica G, *Superconducting MgB$_2$ ceramics and tapes prepared from mechanically milled powders*, J. Optoelec. Adv. Mater. 10 (2008) 2753.

[18] Ma Y, Zhang X, Nishijima G, Watanabe K, Awaji S, Bai XD, *Significantly enhanced critical current densities in MgB$_2$ tapes made by a scaleable nanocarbon addition route*, Appl. Phys. Lett. 88 (2006) 072502.

[19] Bean CP, *Magnetization of Hard Superconductors*, Phys. Rev. Lett. 8, (1962), 250

[20] Homepage of Hypertech Inc, USA: http://www.hypertechresearch.com/.

[21] Groza JR, ASM Handbook Vol. 7: *Powder Metal Technologies and Applications*, eds. Lee PW, Eisen WB, German RM (ASM International Handbook Committee, Ohio), pp. 583-589 (1998).

[22] Lee SY, Yoo SY, Kim YW, Hwang NM, Kim DY, *Preparation of Dense MgB$_2$ Bulk Superconductors by Spark Plasma Sintering*, J. Am. Ceram. Soc. 86, 1800 (2003).

[23] Song KJ, Park C, Kim SW, Ko RK, Ha HS, Kim HS, Oh SS, Kwon YK, Moon SH, Yoo S-I, *Superconducting properties of polycrystalline MgB$_2$ superconductor fabricated by spark plasma sintering*, Physica C 426-431 (2005) 588.

[24] Locci AM, Orru R, Cao G, Sanna S, Congiu F, Concas G, *Simultaneous Synthesis and Densification of Bulk MgB$_2$ Superconductor by Pulsed Electric Current*, AIChE Journal 52(7) (2006) 2618.

[25] S. Ueda, J. I. Shimoyama, A. Yamamoto, S. Horii, K. Kishio, *Enhanced Critical Current Properties Observed in Na$_2$CO$_3$ Doped MgB$_2$*, Supercond. Sci. Technol. 17 (2004) 926.

[26] Perner O, Eckert J, Hassler W, Fischer C, Muller KH, Fuchs G, Holzapfel B, Schultz L, *Microstructure and impurity dependence in mechanically alloyed nanocrystalline. MgB$_2$ superconductors*, Supercond. Sci. Technol. 17 (2004) 1148.

[27] Senkowicz BJ, Giencke JE, Patnaik S, Eom CB, Hellstrom EE, Larbalestier DC, *Improved upper critical field in bulk-form magnesium diboride by mechanical alloying with carbon*, Appl. Phys. Lett. 86 (2005) 202502.

[28] Dou SX, Soltanian S, Horvat J, Wang XL, Zhou SH, Ionescu M, Liu HK, Munroe P, Tomsic M, *Enhancement of the critical current density and flux pinning of MgB$_2$ superconductor by nanoparticle SiC doping*, Appl. Phys. Lett. 81 (2002) 3419.

[29] Jiang X, Ma Y, Gao Z, Yu Z, Nishijima C, Watanabe K, *The effect of different nanoscale material doping on the critical current properties of in situ processed MgB$_2$ tapes*, Supercond. Sci. Technol. 19 (2006) 479.

[30] Yamamoto A, Shimoyama J, Ueda S, Iwayama I, Horii S, Kishio K, *Effects of B$_4$C Doping on Critical Current Properties of MgB$_2$ Superconductor*, Supercond. Sci. Technol. 18 (2005) 1323.

[31] Chen W, Anselmi-Tamburini U, Garay JE, Groza JR, Munir ZA, *Fundamental investigations on the spark plasma sintering/synthesis process: I. Effect of dc pulsing on reactivity*, Mater. Sci. Eng. A 394 (2005) 132.

[32] Aldica G, Badica P, Groza JR, *Field-assisted-sintering of MgB₂ superconductor doped with SiC and B₄C*, J. Optoelec. & Adv. Mater. 9(6) (2007) 1742.

[33] Aldica Gh. –V., Nita P, Tiseanu I, Craciunescu T, Badica P, *High density MgB₂ superconductor: structure and morphology through microtomography and SEM investigations*, J. Optoelec. & Adv. Mater. 10(4) (2008) 929.

[34] Sandu V, Aldica G, Badica P, Groza JR, Nita P, *Preparation pure and doped MgB₂ by field-assisted-sintering technique and superconducting properties*, Supercond. Sci. Technol. 20 (2007) 836.

Superconductor

Edited by Doctor Adir Moyses Luiz

ISBN 978-953-307-107-7

Hard cover, 344 pages

Publisher Sciyo

Published online 18, August, 2010

Published in print edition August, 2010

This book contains a collection of works intended to study theoretical and experimental aspects of superconductivity. Here you will find interesting reports on low-Tc superconductors (materials with Tc< 30 K), as well as a great number of researches on high-Tc superconductors (materials with Tc> 30 K). Certainly this book will be useful to encourage further experimental and theoretical researches in superconducting materials.

How to reference

In order to correctly reference this scholarly work, feel free to copy and paste the following:

Gheorghe Aldica, Ion Tiseanu, Petre Badica, Teddy Craciunescu and Mattew Rindfleisch (2010). X-ray Micro-Tomography as a New and Powerful Tool for Characterization of MgB2 Superconductor, Superconductor, Doctor Adir Moyses Luiz (Ed.), ISBN: 978-953-307-107-7, InTech, Available from: http://www.intechopen.com/books/superconductor/x-ray-micro-tomography-as-a-tool-for-quantitative-characterization-of-mgb2-superconducting-materials

INTECH
open science | open minds